Similarity and difference of the two successive V6 and V7 TRMM multisatellite precipitation analysis performance over China

Sheng Chen,[1,2,3] Yang Hong,[1,2,3] Qing Cao,[2,3] Jonathan J. Gourley,[4] Pierre-Emmanuel Kirstetter,[1,2,3] Bin Yong,[5] Yudong Tian,[6,7] Zengxin Zhang,[8] Yan Shen,[9] Junjun Hu,[1,10] and Jill Hardy[3,4]

Received 5 April 2013; revised 5 November 2013; accepted 10 November 2013; published 11 December 2013.

[1] Similarities and differences of spatial error structures of surface precipitation estimated with successive version 6 (V6) and version 7 (V7) Tropical Rainfall Measuring Mission (TRMM) Multisatellite Precipitation Analysis (TMPA) algorithms are systematically analyzed through comparison with the China Meteorological Administration's national daily precipitation analysis from June 2008 to May 2011. The TMPA products include V6 and V7 real-time products 3B42RTV6 and 3B42RTV7 and research products 3B42V6 and 3B42V7. Both versions of research products outperform their respective real-time counterparts. 3B42V7 clearly improves upon 3B42V6 over China in terms of daily mean precipitation; the correlation coefficient (CC) increases from 0.89 to 0.93, the relative bias (RB) improves from −4.91% to −0.05%, and the root-mean-square error (RMSE) improves from 0.69 mm to 0.54 mm. When considering 3 year mean precipitation, 3B42V7 shows similar spatial patterns and statistical performance to 3B42V6. Both 3B42RTV7 and 3B42RTV6 demonstrate similar bias patterns in most regions of China with overestimation by 20% in arid regions (i.e., the north and west of China) and slight underestimation in humid regions (e.g., −5.82% in southern China). However, 3B42RTV7 overestimates precipitation more than 3B42RTV6 in the cold Qinghai-Tibetan plateau, resulting in a much higher RB of 139.95% (128.69%, 136.09%, and 121.11%) in terms of 3 year annual (spring, summer, and autumn) daily mean precipitation and an even worse performance during winter. In this region, 3B42RTV7 shows an overall slightly degraded performance than 3B42RTV6 with CC decreasing from 0.81 to 0.73 and RB (RMSE) increasing from 21.22% (0.95 mm) to 35.84% (1.27 mm) in terms of daily precipitation.

Citation: Chen, S., et al. (2013), Similarity and difference of the two successive V6 and V7 TRMM multisatellite precipitation analysis performance over China, *J. Geophys. Res. Atmos.*, *118*, 13,060–13,074, doi:10.1002/2013JD019964.

[1]School of Civil Engineering and Environmental Science, University of Oklahoma, Norman, Oklahoma, USA.
[2]Hydrometeorology and Remote Sensing Laboratory, University of Oklahoma, Norman, Oklahoma, USA.
[3]Advanced Radar Research Center, National Weather Center, Norman, Oklahoma, USA.
[4]NOAA/National Severe Storms Laboratory, Norman, Oklahoma, USA.
[5]State Key Laboratory of Hydrology-Water Resources and Hydraulic Engineering, Hohai University, Nanjing, China.
[6]Earth System Science Interdisciplinary Center, University of Maryland, College Park, Maryland, USA.
[7]Hydrological Sciences Laboratory, NASA Goddard Space Flight Center, Greenbelt, Maryland, USA.
[8]Jiansu Key Laboratory of Forestry Ecological Engineering, Nanjing Forestry University, Nanjing, China.
[9]National Meteorological Information Center, China Meteorological Administration, Beijing, China.
[10]School of Computer Science, University of Oklahoma, Norman, Oklahoma, USA.

Corresponding author: Y. Hong, Advanced Radar Research Center, National Weather Center, Suite 4160, 120 David L. Boren Blvd, Norman, OK 73072-7303, USA. (yanghong@ou.edu)

2169-897X/13/10.1002/2013JD019964

1. Introduction

[2] Reliable and accurate measurement and estimation of regional and global precipitation are critical for the applications of meteorology, hydrology, and water resources management. Moreover, precipitation measurement offers essential information in understanding the balance of global energy and water cycle exchanges, which drive most hydrologic models and have direct impacts on the planetary circulation of the atmosphere [*Behrangi et al.*, 2011; *Parkes et al.*, 2013; *Sorooshian*, 2004]. However, reliable and accurate estimation of regional and global precipitation remains a challenge to the scientific community because of the large variability in space and time. The upcoming Global Precipitation Measurement (GPM) mission, which is initiated by the National Aeronautics and Space Administration and the Japan Aerospace Exploration Agency to act as a successor to the existing Tropical Rainfall Measuring Mission (TRMM), is anticipated to be launched in 2014 (http://pmm.nasa.gov/GPM) and will bring us better knowledge of the atmosphere and hydrosphere. Onboard the GPM core satellite will be a multichannel GPM microwave imager (GMI) and a

Ku/Ka-band dual-frequency precipitation radar (DPR). Coupled with currently available sensors and future GPM sensors, a new product named Integrated Multisatellite Retrievals for GPM is anticipated with a better spatiotemporal resolution (0.05° ~ 0.1°/30 min) and quasi-global coverage (60°N–60°S) than current TRMM Multisatellite Precipitation Analysis (TMPA) products (http://ntrs.nasa.gov/archive/nasa/casi.ntrs.nasa.gov/20120015847_2012016148.pdf). Such an ambitious mission will bring more reliable global precipitation products than the current TRMM Multisatellite Precipitation Analysis (TMPA) [*Huffman et al*., 2007] products, and will advance our understanding of Earth's water and energy cycle as well as potentially improve the forecast of extreme events that cause natural hazards and disasters [*Kidd and Huffman*, 2011; *Tapiador et al*., 2012; *Tian et al*., 2007].

[3] Recently, TMPA products have been upgraded from version 6 (V6) to version 7 (V7) that will evolve as the initial version 0 algorithm of the upcoming GPM mission. The TMPA products have two kinds, i.e., the 3 h, real-time, gridded precipitation product (3B42RT) covering the global latitude belt from 60°N to 60°S and a gauge-adjusted, post-real-time research product (3B42) with the coverage of the latitude belt from 50°N to 50°S. Both 3B42RT and 3B42 have a spatial resolution of 0.25° × 0.25°. The V6 3B42 (hereafter, 3B42V6) has been widely applied in the hydrologic and related communities [*Dai*, 2006; *Jiang and Zipser*, 2010; *Li et al*., 2013; *Shepherd*, 2006; *Tobin and Bennett*, 2009], though the product has not been disseminated since 30 June 2011. Similarly, the V6 3B42RT (hereafter, 3B42RTV6) product is no longer available since June 2012. The new V7 TMPA algorithms were released in May 2012 with the 3B42 (hereafter, 3B42V7) product being available since late July 2012, and the real-time product, 3B42RT (hereafter, 3B42RTV7), being available since October 2012. The historic 3B42RTV7 data prior to October 2012 were also retrospectively processed and released in December 2012.

[4] Many previous studies have reported error and uncertainty characteristics of V6 TMPA products [*Chen et al*., 2009; *Gourley et al*., 2010; *Shen et al*., 2010b; *Stampoulis and Anagnostou*, 2012; *Tian et al*., 2010; *Yong et al*., 2012; *Zhou et al*., 2008]. Currently, worldwide ground validation is quite desirable to identify and quantify the similarities and differences of products between the two successive versions as well as the improvement of V7 over V6. This effort will benefit the researchers of hydrology and climatology. For this purpose, a systematic study was conducted by *Chen et al*. [2013] on the spatial error distribution of the V7 TMPA products over the Continental United States. However, to the best of our knowledge, little effort has been reported in evaluating and quantifying the reliability and accuracy of the latest V7 TMPA, reprocessed in late December of 2012, as well as its similarity and difference from the previous V6 products over Mainland China.

[5] The terrain in China is complex. Flat plains predominate the south and east of China, and the west of China features deserts (e.g., the Talamakan Desert, Qaidam Desert, Badain Jaran Desert and Tengger Desert, and Hunshandake Desert) and mountains with high-altitude plateaus (e.g., the Qinghai-Tibet plateau). The Asian monsoon represents one specific characteristic of precipitation in China. The monsoon brings a large amount of humid air contributing to most of the precipitation in China. The annual precipitation amount gradually decreases from the southeast to the northwest with an exception in Qinghai-Tibetan plateau due to the complexity of the terrain there. Accurate estimation of the precipitation in Qinghai-Tibetan plateau is still a great challenge to the hydrometeorology community [*Bajracharya et al*., 2008] because of the serious beam blockages from ground radars [*Gjertsen and Haase*, 2005] and the limitations of spaceborne retrievals [*Iguchi et al*., 2000; *Smith and Kummerow*, 2013]. The primary objective of this study is to quantify the error characteristics of V7 TMPA as well as the differences between V6 and V7 over China. The real-time product 3B42RT and post-real-time research quality product 3B42 are assessed in terms of spatial distribution, temporal variation, and frequency of precipitation with various intensities. The results are useful to guide TMPA users' data applications in China and are helpful for TMPA algorithm developers to improve the spaceborne retrieval algorithm, especially for the high-altitude Tibetan Plateau, high-latitude area and inland central Asia.

[6] The paper is organized as follows. Section 2 introduces 3 year precipitation data sets, rainfall algorithms, and evaluation metrics. Section 3 provides an analysis of the spatial characteristics and error quantification of V6 and V7 TMPA products. Scatter plots, probability distribution functions (PDFs), contingency metrics, daily correlation coefficient (CC), and area-mean precipitation are utilized in the assessment. A summary of results and the conclusions are provided in section 4.

2. Study Region and Data

[7] Figure 1 shows the topographic distribution through a digital elevation model representation. China can be roughly separated into three regions based on the elevation: (1) >3000 m, (2) 1000–3000 m, and (3) <1000 m. Considering the annual mean precipitation distribution [*Qian and Lin*, 2005], mountain ranges [*Tang et al*., 2006], and elevations, eight subregions are defined in Figure 1: (1) the inland Xinjiang (XJ) region in central Asia, which is characterized by an arid to semiarid climate, (2) the Qinghai-Tibetan plateau (QZ) at high altitude, (3) Northwestern China (XB) bounded by the 400 mm annual rainfall isohyet; (4) Northeastern China (DB) north of Mountain Yan; (5) Northern China (HB) north of Qinling Mountain and the Huai River; (6) the plain region of Changjiang (Yangtze) River (CJ); (7) the southwest Yungui Plateau (YG) bounded by the Dabashan Mountains to the north and Wulingshan Mountains to the east; and (8) southeastern China (HN) south of the Nanling Mountains and southeast of the Wuyishan Mountains.

[8] Precipitation in the inland XJ region is mainly a result of moisture advected by the midlatitude westerlies coming from the North Atlantic Ocean [*Bothe et al*., 2012]. The monsoon brings a large amount of humid air from the Indian and Pacific Oceans to the southwestern, southern, and southeastern parts of China, where the interception of humid air by the complex terrain generally produces heavy precipitation. The climate of southern and southeastern China is mainly influenced by the monsoon, which moves back and forth between the Siberia-Mongolian Plateau and the Pacific Ocean. This seasonal propagation of the monsoon results in the Mei-yu from June to July in these areas [*Shen et al*., 2010b] and assists in typhoon formation in the western Pacific Ocean and subsequent landfall in southern and southeastern China [*Liang*, 2012]. The monsoon between the Qinghai-Tibetan (QZ) plateau and the

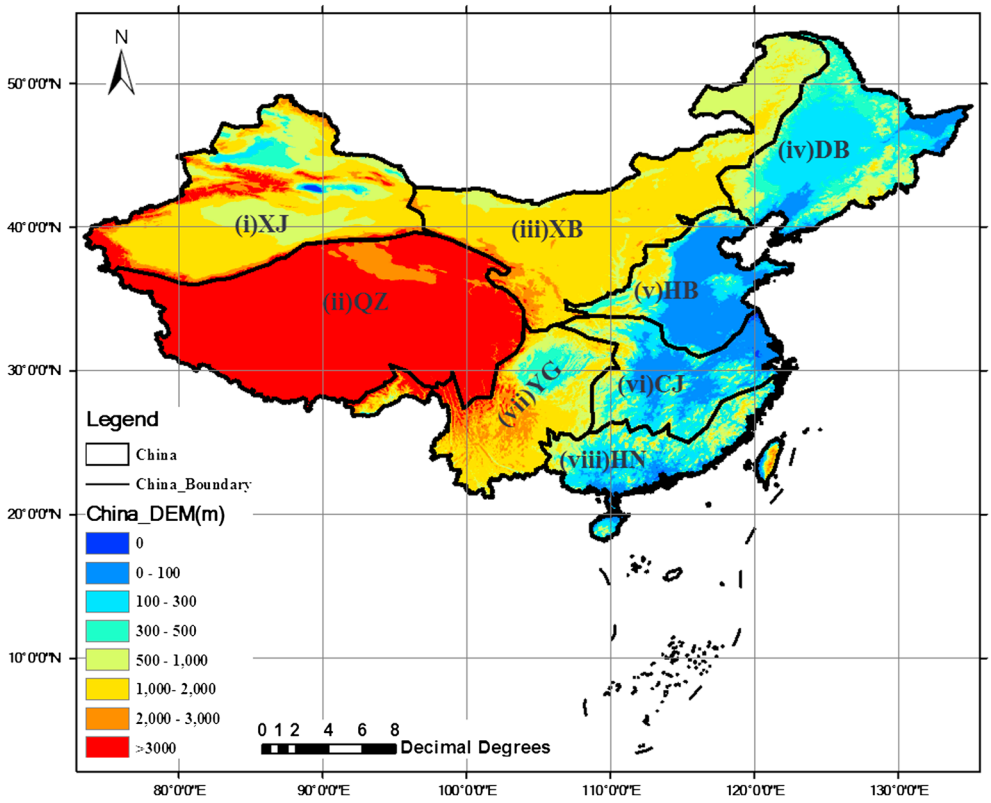

Figure 1. Topographic features in China. The solid black line indicates the outline of the subregions: (i) Xinjiang (XJ), (ii) Qinghai-Tibetan plateau (QZ), (iii) Northwest (XB), (iv) Northeast (DB), (v) North (HB), (vi) Middle and lower reaches of Changjiang River (CJ), (vii) southwest Yungui Plateau (YG), and (viii) Southeast (HN).

Indian Ocean is the major factor affecting the climate of southwestern China.

[9] The gauge-based hourly precipitation product of China is not available to the public. However, the newly released high-resolution (0.25° × 0.25° latitude/longitude) China daily Precipitation Analysis Products (CPAP) developed by the National Meteorological Information Center and China Meteorological Administration can be accessed [*Shen et al*., 2010a], and, therefore, have been used as the ground reference in this study. Regarding CPAP, an optimal interpolation (OI) technique driven by the Parameter-Elevation Regression on Independent Slopes Model (PRISM; [*Daly et al*., 1994; *Shen et al*., 2010a]), is applied to interpolate the 2419 daily gauge measurements to a 0.25° gridded domain (http://cdc.cma.gov.cn/dataSetDetailed.do). The OI technique yields a higher correlation with individual gauge measurements than the other techniques [*Chen et al*., 2008]. A validation experiment shows that CPAP's relative bias (RB) is 3.21% at 0.5° scale when compared to independent gauge observations [*Shen et al*., 2010a].

[10] The TMPA algorithm merges a variety of satellite-based observations and ground observations to yield high spatiotemporal resolution and quasi-global quantitative precipitation estimation (QPE) products. It relies on two types of satellite sensors, i.e., microwave (MW) and infrared (IR). The MW sensors include TRMM Microwave Imager (TMI), Special Sensor Microwave Imager (SSMI), Special Sensor Microwave Imager/Sounder (SSMI/S, for 3B42V7 only), Advanced Microwave Scanning Radiometer-EOS (AMSR-E), Advanced Microwave Sounding Unit B (AMSU-B), and Microwave Humidity Sounder. The IR sensors applied by TMPA come from all available geostationary satellites (GOES, METEOSAT, and GMS/MT-SAT series). The precipitation product estimated from MW data is named 3B40RT (high quality, or HQ) and is used to calibrate the IR-based product 3B41RT (variable rain rate, or VAR). In cases where HQ data do not exist, VAR data are used to fill in the field. The combination of HQ and VAR data forms the real-time QPE product 3B42RT. Three additional data sources employed to generate post-real-time TMPA products include the following: (1) the TRMM Combined Instrument (TCI) estimate that combines the data from TMI and the precipitation radar (PR) (TRMM product 2A31); (2) the Global Precipitation Climatology Center (GPCC) 1° monthly full/monitoring gauge product; and (3) the Climate Assessment and Monitoring System (CAMS, V6 only) 0.5° × 0.5° monthly gauge product. The monthly ratio of the rainfall accumulation calculated from satellite-only and from satellite-gauge combination is applied to adjust the 3-hourly accumulations in the month to produce the 3B42 product. In addition, the 0.07° Grisat-B1 infrared data have been included in 3B42V7 during the period of 1998–1999, leading to a significant improvement in resolution and areal coverage over 3B42V6. 3B42V7 incorporates the new GPCC "full" gauge analysis whenever it is available and the GPCC "monitoring" gauge analysis since 2010. For V6, the previous GPCC monitoring product was used up through April 2005, and then the CAMS analysis was used thereafter [*Huffman et al*., 2011]. The major changes from V6 to V7 are summarized next.

[11] First, the enhanced TRMM Level-2 PR product has been used in V7. Studies by *Chen et al.* [2012a] and *Kirstetter et al.* [2013] showed that the V7 Level-2 PR product (i.e., 2A25 or PRV7) gained small to moderate improvements over the V6 Level-2 PR product (i.e., 2A25 or PRV6). Second, V7 TMPA makes use of the GPCC data with improved climatology and anomaly analysis, especially in complex terrain [*Huffman et al*., 2011]. Third, V7 blends more satellite data, including SSMI/S and 0.07° Grisat-B1 infrared data, which represent an improvement in resolution and areal coverage over the infrared data (1°/24 classes) used in the V6 algorithm. More details can be seen in *Huffman et al*. [2011] and *Huffman and Bolvin* [2013].

[12] In order to be temporally consistent with the daily CPAP product, the TMPA 3 h precipitation products have been accumulated into daily precipitation estimates starting from 00 UTC. To compute the daily rainfall from TMPA rainfall rate, the rainfall rates at 0000 UTC and 2400 UTC were accumulated for 1.5 h while rainfall rates at other times (i.e., 0300, 0600, 0900, 1200, 1500, 1800, and 2100 UTC) were accumulated for 3 h. Since CPAP starts from April 2008 and 3B42V6 ends in June 2011, this study has chosen QPE products from June 2008 to May 2011. The readers should bear in mind that the gauges used in CPAP are not be completely independent from those used in 3B42V7, since there are approximately 500 out of the total 2419 gauges that are potentially used in both the GPCC and CPAP data sets according to the China Meteorological Administration (http://cdc.cma.gov.cn/dataSetDetailed.do). Statistical evaluation metrics include the following: Bias (the difference between the TMPA and the reference), RB (the Bias divided by the reference), root-mean-square error (RMSE), and the Pearson linear correlation coefficient (CC). RB, when multiplied by 100, denotes the degree of overestimation or underestimation in percentage. All the statistics have been computed on a pixel-by-pixel basis over China.

3. Result Analysis

3.1. Three Year Daily Mean Precipitation

[13] Figures 2a–2f show the gauge density and 3 year mean precipitation for TMPA and CPAP products. Gauge stations are dense in eastern China and relatively sparse in some areas in NW, XJ, and QZ. V6 and V7 TMPA products generally capture the spatial pattern of precipitation over China, but their differences are notable. 3B42V6 and 3B42V7 have a very similar precipitation distribution to CPAP. However, 3B42V6 seems to underestimate the rainfall along the southwest border of China, i.e., southeast of QZ and southwest of YG. Both 3B42RTV7 and 3B42RTV6 estimate a large amount of precipitation in the Qinghai-Tibetan Plateau, which is southeast and upwind of the Tianshan Mountains in northwestern XJ. Impressively, 3B42RTV7 shows much more precipitation than 3B42RTV6 in the mountainous areas, especially in southern QZ. In the desert areas (e.g., the Taklamakan Desert and Hunshandake Desert) and the other plain areas in XJ and XB, 3B42RTV7 shows less precipitation than 3B42RTV6. It is noted that both 3B42RTV7 and 3B42V7 show many isolated grid boxes of abnormal overestimation, particularly in northeastern China. Qualitatively, 3B42V7 performs better than 3B42V6, while 3B42RTV7 is a little worse than 3B42RTV6.

[14] Figures 2g–2j show a quantitative comparison of TMPA versus CPAP for 3 year daily mean precipitation over the entire Mainland China. The density-colored scatter plots suggest that the research products perform much better than the real-time products in terms of RB, RMSE, and CC. Meanwhile, 3B42V7 performs much better than its counterpart 3B42V6. Among the four products, 3B42V7 has the highest CC (0.93), a small RB (−0.05%), and the smallest RMSE (0.54 mm). 3B42V6 has a slightly lower CC (0.89), a worse RB (−4.91%), and a larger RMSE (0.69 mm). The other two products, 3B42RTV7 and 3B42RTV6, have a much higher positive bias and RMSE. Table 1 provides more detailed statistics for the eight subregions. It is worth noting that both 3B42RTV6 and 3B42RTV7 heavily overestimate the precipitation in the arid and semiarid XJ (134.14% and 129.82%, respectively) and XB regions (66.59% and 49.87%, respectively). The possible reasons are given as follows. First, hydrometeors that are detected by the microwave and infrared sensors as well as the precipitation radar onboard the satellites [*Story et al*., 2001; *Surussavadee and Staelin*, 2010] might partially or totally evaporate before they reach the surface during the warm season. Second, it is difficult for SSMI-type sensors to uniquely identify the precipitation over arid regions due to the land surface properties of the desert and its impact on the upwelling microwave radiation [*Grody and Weng*, 2008]. Third, the gauge stations are relatively sparse in some areas of XJ and XB, which may allow the OI scheme to spread nonzero precipitation into zero precipitation areas.

[15] Overestimation by 3B42RTV6 and 3B42RTV7 also can be seen in QZ with overestimations of 64.49% and 139.95% for 3B42RTV6 and 3B42RTV7, respectively. This fact implies that the real-time TMPA algorithms have great uncertainty in estimating the precipitation in high-altitude plateaus. A study by *Amitai et al*. [2004] showed that the overcorrection of attenuation for PR's reflectivity might lead to the overestimation. Because PR's reflectivity is an important component of the monthly rainfall product 2B31 that is used to calibrate the retrievals from passive MW (PMW) sensors and thereafter the IR data, the overcorrection of attenuation may lead to 3B42RTV7's worse performance than 3B42RTV6. In addition, PR has difficulties in accurately estimating rainfall in high-altitude regions because of the bright band and/or ground clutter contamination [*Fu and Liu*, 2007]. According to the statistics in other subregions, 3B42V7 shows a significant improvement over 3B42V6, whereas the improvement of 3B42RTV7 over 3B42RTV6 is not apparent. It is likely that the effective usage of GPCC "full" gauge analysis and improved climatology and anomaly analysis (especially in complex terrain) significantly improves the V7 research products. In DB, which is beyond the coverage (38°S–N) of TRMM, both 3B42RTV7 and 3B42V7 demonstrate a better performance than their V6 counterparts with smaller RBs (14.23% versus 28.84% and 15.38% versus 13.80%) and higher CCs (0.54 versus 0.52 and 0.91 versus 0.89), respectively. This result indicates that the V7 TMPA gains moderate improvement in the high-latitude areas. The overestimation of real-time TMPA products in DB is likely due to frozen precipitation primarily in winter because HQ has some limitations in estimating precipitation in regions with frozen or icy surfaces [*Huffman and Bolvin*, 2013]. The PMW-based retrievals, e.g., AMSR-E and AMSU-B

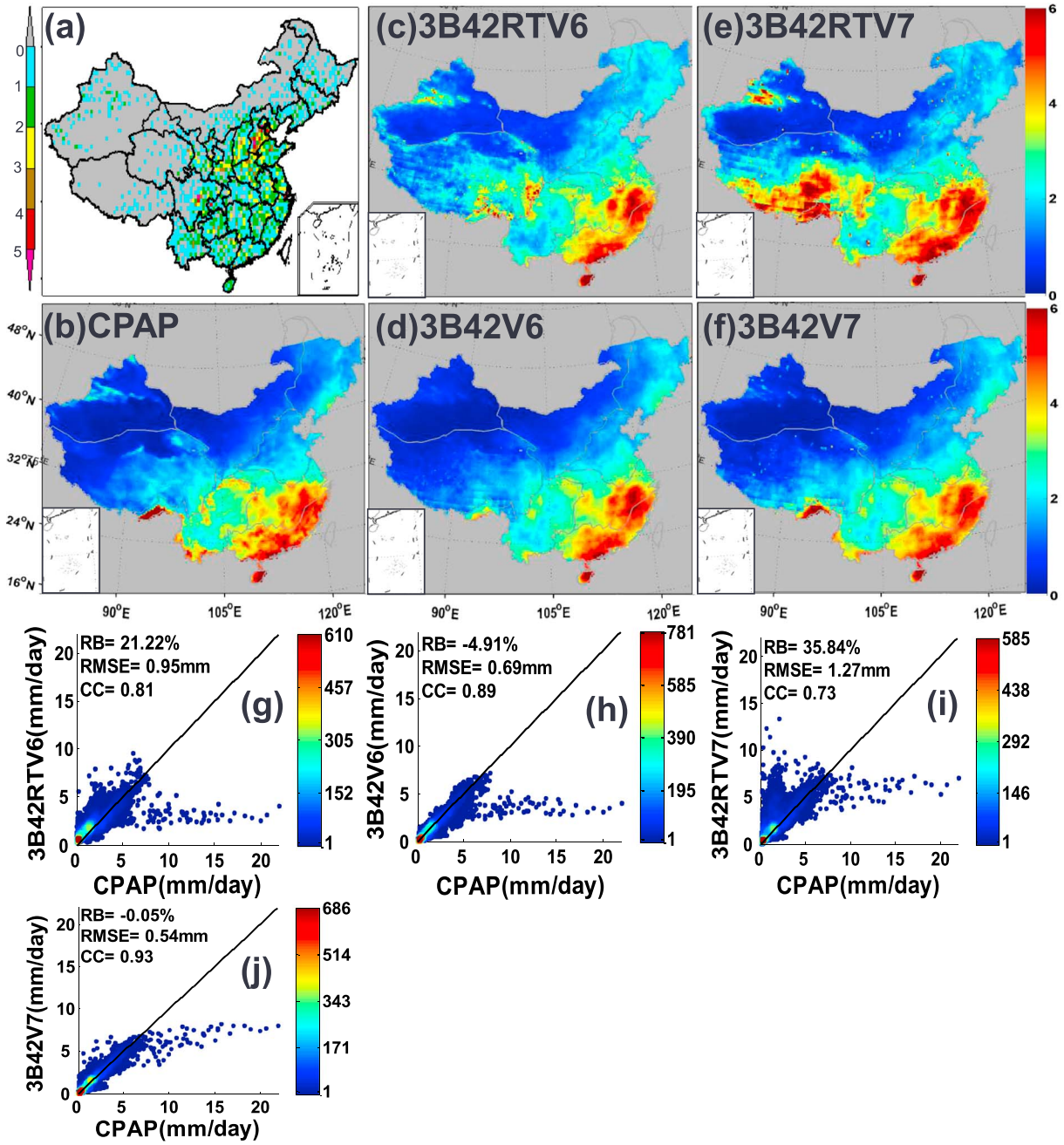

Figure 2. (a) A 0.5° × 0.5° density map of gauges used in CPAP. 2419 gauges were used in CPAP. (b–f) Three year daily mean rainfall of V6/V7 TMPA over China, and (g–j) density-colored scatter plots of TMPA versus CPAP.

beyond 38°N–S, are also degraded by snow cover [*Ferraro et al*., 1998; *Grody*, 1991]. AMSU-B's high frequency channels (89 and 150 GHz) can detect more scattering signals from ice particles in the atmosphere and therefore may overestimate precipitation rates in winter [*Vila et al*., 2007; *Yong et al*., 2010]. In addition, the IR-based 3B41RT, which is used to fill the gaps in case HQ is not available [*Huffman and Bolvin*, 2013], has limitations as well in estimating precipitation in complex terrain [*Chen et al*., 2012b; *Hirpa et al*., 2010; *Negri and Adler*, 1993; *Tuttle et al*., 2008], especially for warm top stratiform cloud systems during the cold season [*Tian et al*., 2007; *Vicente et al*., 1998].

3.2. Seasonal Daily Mean Precipitation

[16] Northwestern China is characterized by an arid to semiarid climate, and southeastern China is dominated by the monsoon. Figure 3 shows China's seasonal daily mean precipitation derived from CPAP and TMPA, and Figure 4 shows the density-colored scatter plots of TMPA versus CPAP. Seasonal statistics for the eight subregions are listed in Table 1. Both 3B42V6 and 3B42V7 show similar spatial patterns to CPAP. 3B42V7 demonstrates better estimation than 3B42V6 around the southwest border of China where 3B42V6 underestimates precipitation most notably in summer and autumn. 3B42V6 has a very small RB (−0.34%) in summer and fairly small

Table 1. RB, RMSE, and CC for Annual and Seasonal Precipitation for Each Region[a]

Indexes	Time	Type	China	XJ	QZ	XB	DB	HB	CJ	YG	HN
RB (%)	3 years	3B42RTV6	21.22	134.14	64.49	66.59	28.84	27.42	−0.99	−25.03	−5.82
		3B42V6	−4.91	−31.88	−8.09	10.63	13.80	11.03	2.06	−23.58	−5.82
		3B42RTV7	35.84	129.82	139.95	49.87	14.23	22.35	7.45	−11.62	2.95
		3B42V7	−0.05	−28.42	3.09	10.00	15.38	10.51	1.89	−12.63	−2.47
	Spring	3B42RTV6	9.82	47.62	66.58	67.70	6.21	22.10	−9.13	−21.83	−3.97
		3B42V6	−6.34	−37.43	−6.86	15.26	12.76	8.91	−1.67	−26.09	−4.74
		3B42RTV7	14.98	82.53	128.69	41.83	−16.12	7.98	−7.61	−19.84	−4.94
		3B42V7	−2.20	−32.44	9.79	10.57	12.52	7.38	−2.63	−14.52	−3.51
	Summer	3B42RTV6	9.86	144.41	13.36	36.14	7.33	16.92	11.86	−24.38	3.21
		3B42V6	−0.34	−21.66	−6.05	12.91	8.78	13.22	10.65	−18.25	1.59
		3B42RTV7	44.24	190.68	136.09	49.34	9.50	23.72	23.35	−6.11	17.48
		3B42V7	3.37	−18.68	1.58	12.57	11.02	11.36	8.37	−8.28	3.62
	Autumn	3B42RTV6	18.77	49.46	91.36	54.38	53.12	29.12	−12.98	−32.03	−21.49
		3B42V6	−12.42	−46.56	−14.62	2.76	20.69	5.99	−5.01	−28.78	−12.48
		3B42RTV7	35.62	105.39	121.11	46.66	45.41	22.99	9.03	−14.24	−4.91
		3B42V7	−4.95	−43.40	−5.89	5.27	26.67	9.74	−0.17	−16.45	−4.30
	Winter	3B42RTV6	167.41	456.29	1341.99	609.79	306.27	165.66	−9.97	−10.84	−27.22
		3B42V6	−13.44	−15.97	−8.13	9.94	59.33	10.87	−10.03	51.56	−36.27
		3B42RTV7	42.94	113.81	569.25	123.18	98.22	54.15	−14.43	−26.12	−33.26
		3B42V7	−4.74	−13.64	96.70	3.01	47.31	14.21	−7.43	−38.85	−29.02
RMSE	3 years	3B42RTV6	0.95	0.76	0.94	0.62	0.59	0.62	0.45	2.09	0.68
		3B42V6	1.27	0.37	0.35	0.16	0.30	0.33	0.40	1.94	0.66
		3B42RTV7	0.69	1.06	2.00	0.60	0.45	0.61	0.59	1.62	0.70
		3B42V7	0.54	0.33	0.46	0.20	0.30	0.32	0.34	1.35	0.50
	Spring	3B42RTV6	0.97	0.47	0.85	0.50	0.42	0.48	0.78	2.28	1.09
		3B42V6	0.78	0.47	0.30	0.16	0.32	0.28	0.52	2.24	0.72
		3B42RTV7	1.06	0.91	1.30	0.65	0.49	0.54	0.85	1.87	0.85
		3B42V7	0.63	0.43	0.42	0.27	0.33	0.29	0.46	1.65	0.60
	Summer	3B42RTV6	1.73	1.32	1.38	0.88	1.00	1.29	1.53	4.00	1.66
		3B42V6	1.36	0.44	0.91	0.40	0.64	0.95	1.17	3.57	1.49
		3B42RTV7	3.12	2.32	5.26	1.26	1.02	1.55	1.96	2.93	2.34
		3B42V7	1.10	0.45	1.13	0.45	0.64	0.85	0.97	2.37	1.26
	Autumn	3B42RTV6	1.09	0.62	1.40	0.59	0.61	0.58	0.66	2.09	1.05
		3B42V6	0.73	0.53	0.57	0.22	0.28	0.28	0.40	1.85	0.89
		3B42RTV7	1.18	1.21	1.59	0.68	0.60	0.70	0.69	1.71	0.93
		3B42V7	0.62	0.49	0.59	0.27	0.33	0.28	0.34	1.43	0.69
	Winter	3B42RTV6	1.09	1.34	1.47	0.79	1.01	0.79	0.69	0.64	0.68
		3B42V6	0.32	0.33	0.11	0.08	0.27	0.18	0.49	0.55	0.63
		3B42RTV7	0.58	0.58	0.67	0.22	0.35	0.48	0.76	0.69	0.76
		3B42V7	0.30	0.32	0.21	0.07	0.22	0.17	0.43	0.47	0.55
CC	3 years	3B42RTV6	0.81	0.79	0.74	0.80	0.52	0.74	0.89	0.29	0.80
		3B42V6	0.89	0.82	0.87	0.96	0.89	0.88	0.91	0.52	0.75
		3B42RTV7	0.73	0.73	0.56	0.69	0.54	0.71	0.85	0.63	0.72
		3B42V7	0.93	0.80	0.79	0.92	0.91	0.88	0.93	0.84	0.83
	Spring	3B42RTV6	0.85	0.76	0.66	0.78	0.05	0.73	0.93	0.52	0.81
		3B42V6	0.91	0.70	0.88	0.94	0.57	0.90	0.96	0.60	0.90
		3B42RTV7	0.83	0.65	0.50	0.43	0.15	0.66	0.90	0.72	0.87
		3B42V7	0.94	0.73	0.80	0.80	0.64	0.88	0.97	0.82	0.92
	Summer	3B42RTV6	0.81	0.79	0.79	0.84	0.61	0.59	0.64	0.29	0.67
		3B42V6	0.88	0.72	0.85	0.95	0.89	0.80	0.74	0.50	0.68
		3B42RTV7	0.67	0.67	0.61	0.74	0.63	0.59	0.71	0.64	0.57
		3B42V7	0.93	0.75	0.80	0.93	0.92	0.83	0.77	0.85	0.78
	Autumn	3B42RTV6	0.64	0.67	0.57	0.69	0.16	0.70	0.50	0.20	0.94
		3B42V6	0.85	0.71	0.64	0.89	0.79	0.78	0.76	0.47	0.95
		3B42RTV7	0.67	0.70	0.39	0.58	0.18	0.62	0.53	0.43	0.93
		3B42V7	0.88	0.70	0.62	0.86	0.79	0.81	0.81	0.73	0.95
	Winter	3B42RTV6	0.19	0.04	−0.26	0.24	0.21	0.50	0.69	0.27	0.57
		3B42V6	0.85	0.48	0.22	0.68	0.71	0.90	0.87	0.26	0.83
		3B42RTV7	0.56	0.10	0.14	0.45	0.44	0.46	0.70	0.18	0.56
		3B42V7	0.87	0.55	0.24	0.66	0.75	0.90	0.89	0.49	0.82

[a]RB, relative bias; RMSE, root-mean-square error; and CC, correlation coeficient.

underestimation for the other three seasons. The CC value of 3B42V6 is high (≥ 0.85). Compared to 3B42V6, 3B42V7 gives a higher CC and less underestimation for each season, except that it slightly overestimates precipitation by 3.37% in summer, whereas 3B42V6 underestimates by −0.34%. 3B42RTV6 and 3B42RTV7 have relatively worse performance than their respective research products 3B42V6 and 3B42V7. They generally overestimate precipitation amounts. In comparison, 3B42RTV7 has a larger overestimation than 3B42RTV6 in spring, summer, and autumn, while during the wintertime, 3B42RTV6 shows an abnormal overestimation (167.41%) and a very low CC (0.19). It is also noted that both 3B42RTV6 and 3B42RTV7 show significant differences with CPAP in

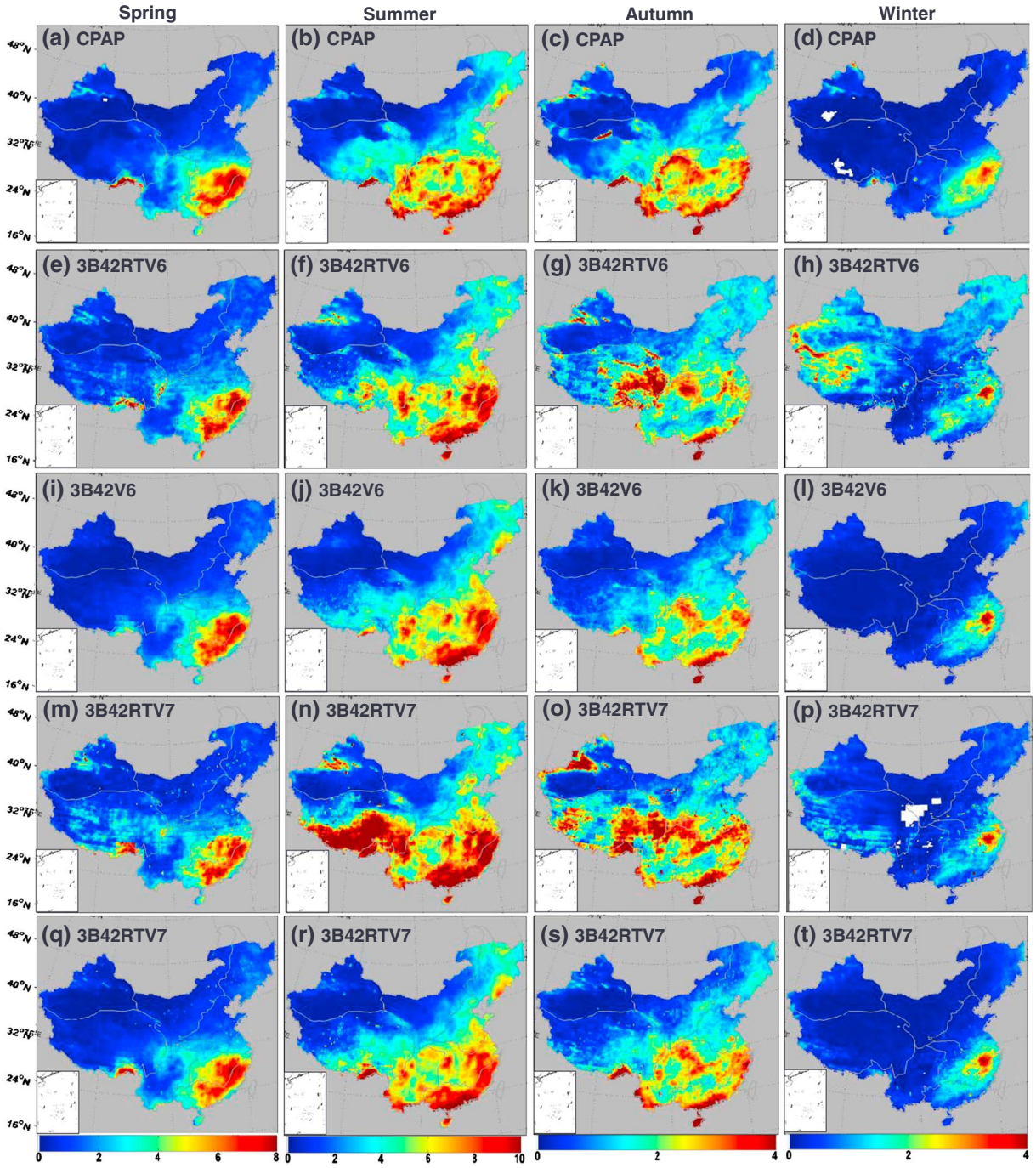

Figure 3. Seasonal daily mean precipitation distributions over China for V6 and V7 TMPA products and CPAP.

XJ, QZ, and HB regions where 3B42RTV7 overestimates more than 3B42RTV6 in summer and autumn, but less so in winter (Table 1). The large overestimation is likely due to the above mentioned limitations of the TRMM-PR algorithm, HQ algorithms, and the IR-based 3B41RT. In southeastern China, the coastal mountains intercept the humid air masses from the Pacific Ocean and the cold air masses coming from the northwest, producing a large amount of precipitation there. It is noted that all the TMPA products overestimate rainfall in this region during summer. This is very likely attributed to the aforementioned limitation of the IR-based 3B41RT [*Huffman and Bolvin*, 2013].

3.3. Daily Precipitation

[17] Figure 5 shows the temporal behavior of the daily bias, CC and RMSE of TMPA products over Mainland China and its eight subregions. The CC and RMSE generally show an annual periodic variation and a high correlation with each other, although this trend is not clearly seen for the daily bias. Similarly, all four TMPA products have an obvious correlation among them in terms of CC and RMSE, while the

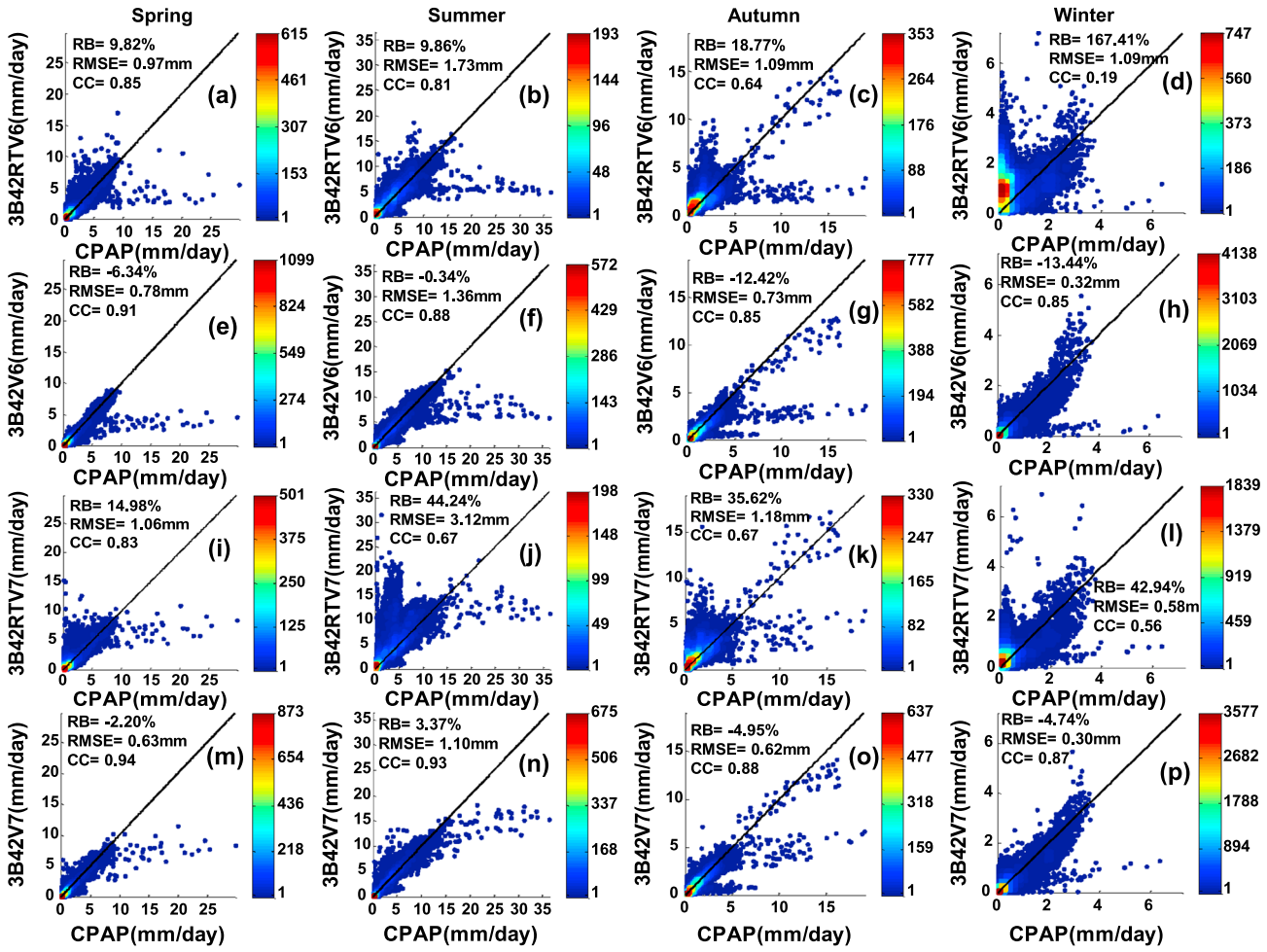

Figure 4. Scatter plots of TMPA versus CPAP for different seasonal daily mean precipitation over China.

daily bias values show a large fluctuation. The highest (lowest) CC values normally appear in July/August (December/January), and the RMSE values have the same trend with an exception in the XJ region. This result suggests that seasonal precipitation and land surface characteristics impact the TMPA error. In terms of Bias, CC, and RMSE, the post-real-time research quality product 3B42 outperforms the real-time product 3B42RT. 3B42V7 shows a better performance than 3B42V6, while 3B42RTV6 demonstrates better estimation than 3B42RTV7. In QZ, 3B42RTV7 appears to overestimate much more than 3B42RTV6, especially in summer. The large overestimation of 3B42RTV7 in QZ is the major reason for 3B42RTV7's worse performance during summertime as indicated by the statistics of the whole region (Figure 5a). In addition, as shown in the first column of Figure 5, the V6 products show notable underestimated precipitation before 2009 (Figure 5a). Since 2009, 3B42RTV6 shows prominent overestimation in spring and autumn while 3B42V6 shows very small bias. This change in the error behavior is very likely due to the addition of the climatological TCI and 3B43 calibrations to the TMPA-RT algorithm since October 2008 [*Huffman et al.*, 2010; *Yong et al.*, 2012].

[18] It is worth noting that both V6 and V7 products show an evident underestimation in YG almost all the time, especially during summer and autumn. The YG region has much less precipitation in every season (Figure 3) than CJ and HN in the east. The reasons behind this can be explained as follows. In the rainy season, the moisture in the air masses is greatly reduced after the Indian monsoon climbs over the Hengduan Mountains in southwestern YG. The air masses adiabatically sink in the lee of the mountains and spread northwestward. The northerly cold air is impeded by the Dabashan Mountains and Wulingshan Mountains in the northeast of YG and moves slowly southwestward into the complex YG plateau. The convergence of cold and warm air in the complex terrain can produce shallow, orographic rainfall. This type of rainfall system tends to be underestimated by the passive microwave radiometer algorithms because of the weak ice scattering signatures [*Shige et al.*, 2012; *Todd and Bailey*, 1995] and is poorly estimated by IR techniques as well [*Sakakibara*, 1981; *Takao and Kunio*, 1980].

3.4. Probability Distributions by Occurrence and Precipitation Volume

[19] Precipitation has large variability in space, time, and intensity over China. Heavy precipitation is often observed in southeast coastal areas, which are normally influenced by the monsoon and typhoons. Probability distribution functions (PDFs) are good tools to help us understand the relations among precipitation rate, precipitation volume, and

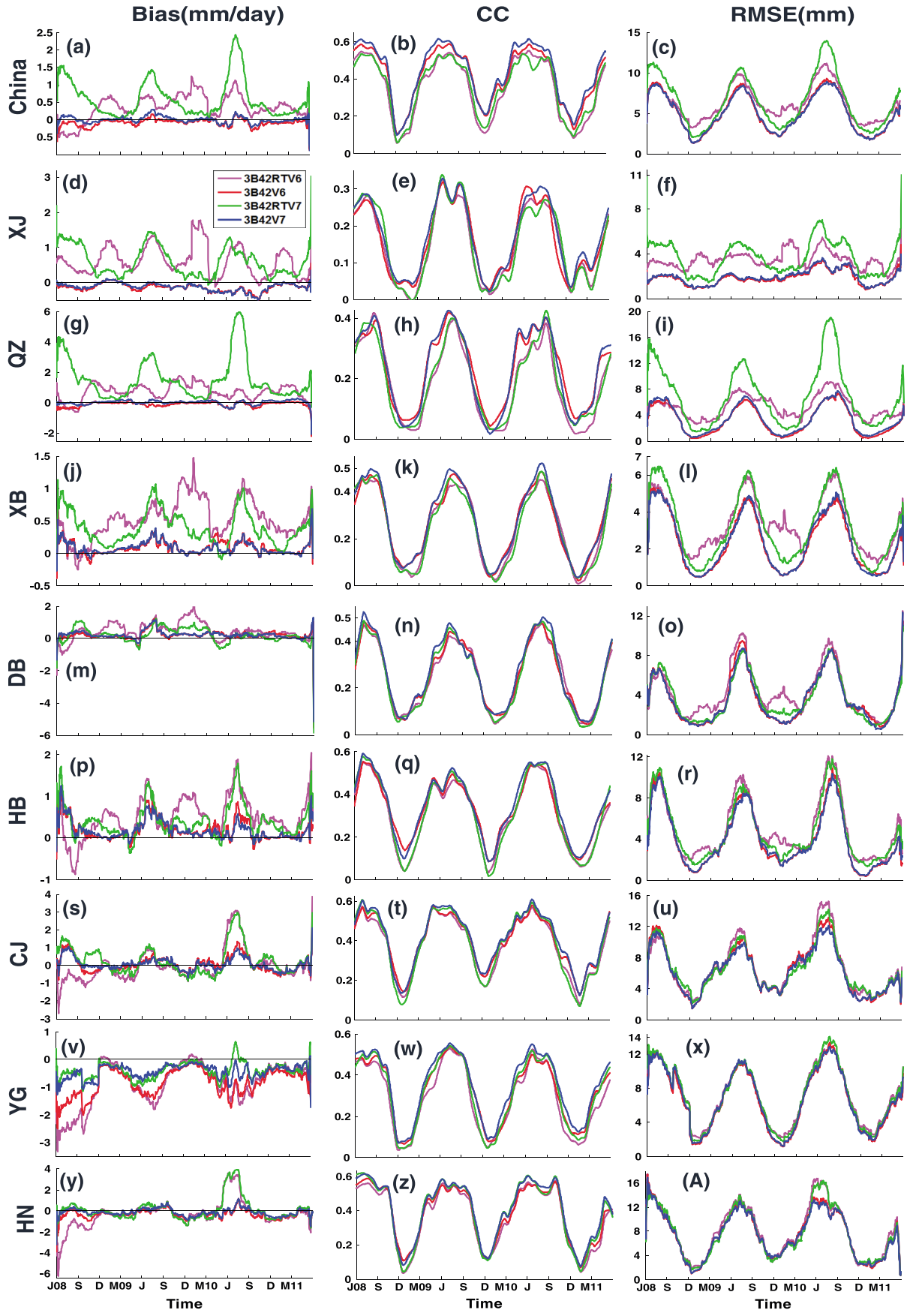

Figure 5. Daily series of Bias, CC, and RMSE for mean precipitation in China and eight subregions. Vertical axis scales were set according to the maximum of *y* axis in different subpanels.

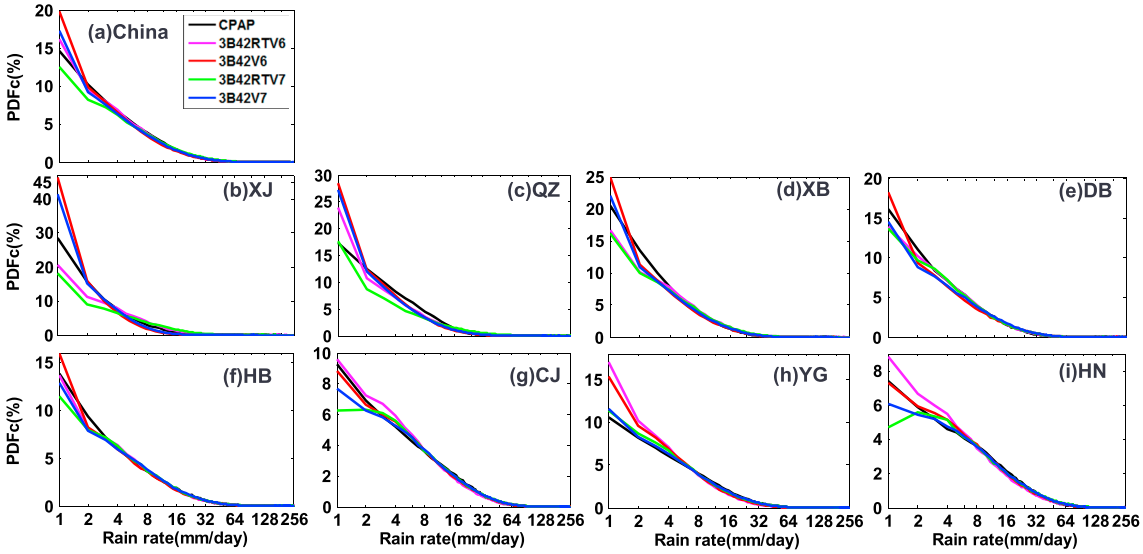

Figure 6. Probability distribution functions by occurrence (PDFc) for different regions, which are derived using a 1 mm/day interval. Vertical axis scales were set according to the maximum of *y* axis in different subpanels.

estimation sensitivity. In addition, PDFs offer an insight into the error dependence on precipitation rate as well as the potential error impact on hydrological applications [*Tian et al.*, 2010]. Figures 6 and 7 show the daily precipitation PDFs by occurrence (PDFc) and the PDFs by volume (PDFv), respectively, for TMPA and CPAP. The computation of PDFc and PDFv has only been performed at grid cells where both the reference and TMPA have nonzero rainfall estimates.

[20] As shown in Figures 6 and 7, the V6 and V7 products generally have similar distribution patterns in terms of precipitation rates for both the occurrence and the volume of precipitation. The main difference of PDFc is evident at the lower end (<4 mm/day) where 3B42RTV7 obviously underdetects light rainfall (<4 mm/day), especially in XJ, QZ, and XB. In XJ, the 3B42 products seem to have less precipitation for rates greater than 4 mm/day, and the real-time products appear to yield much less (more) precipitation for rates lower (greater) than 4 mm/day (Figure 7b). In QZ, the 3B42 products have less precipitation for rates between 2 mm/day and 24 mm/day and more precipitation for rates greater than 32 mm/day (Figure 7c). The 3B42RTV7 distinctly estimated much less (more) precipitation for rates lower (greater) than 16 mm/day. In XB, all the TMPA products underestimate precipitation rates less than 4 mm/day. Figures 7b–7d suggest that it is still a great challenge for accurate satellite-based QPE in the high-altitude mountainous region and remote desert areas.

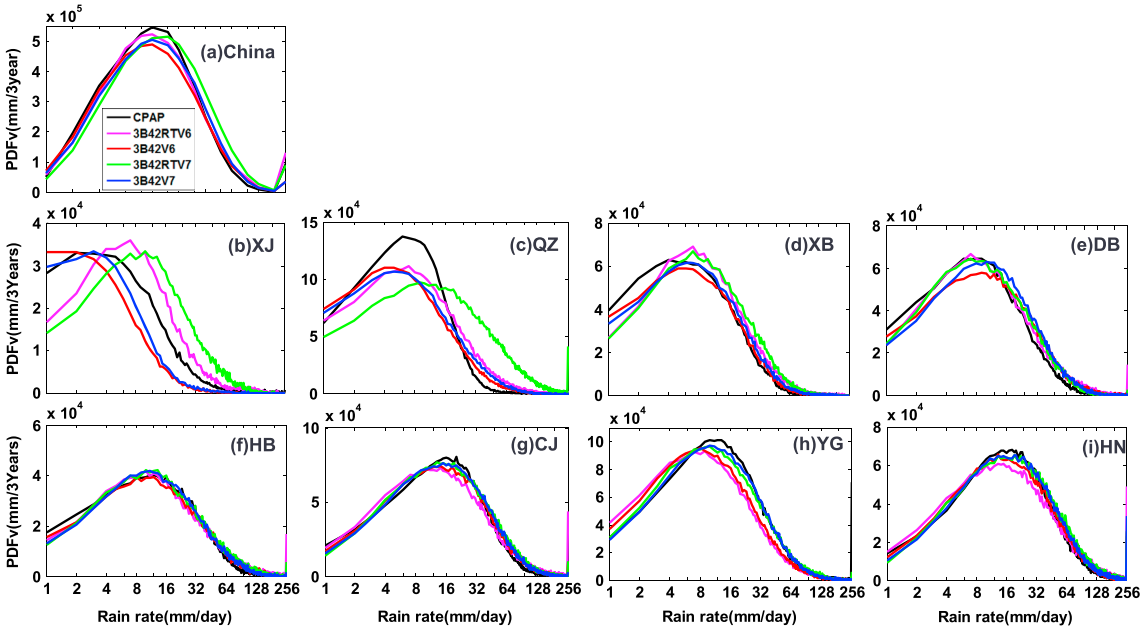

Figure 7. Probability distribution functions by volume (PDFv) for different regions, which are derived using a 1 mm/day interval. Vertical axis scales were set according to the maximum of *y* axis in different subpanels.

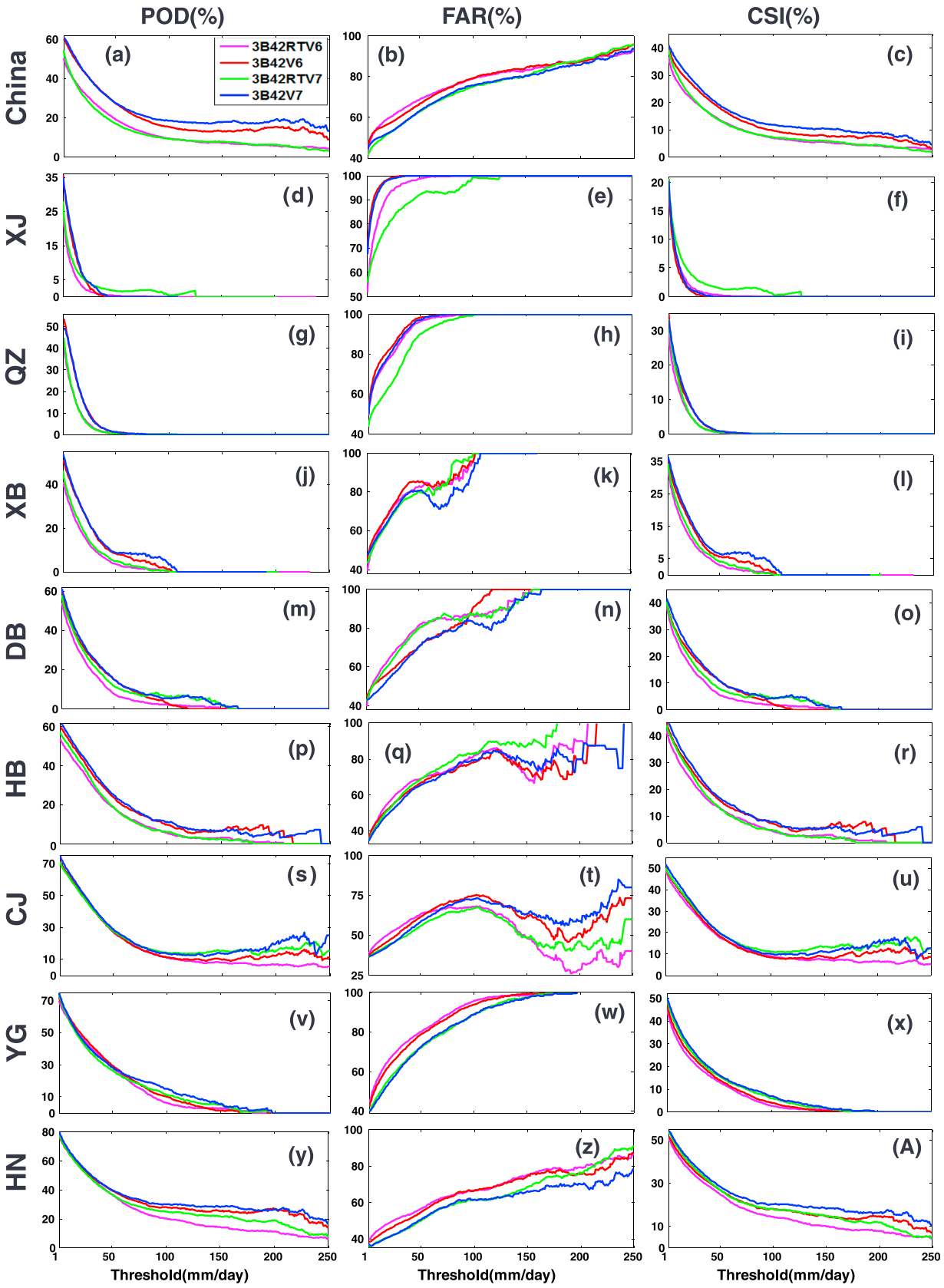

Figure 8. Contingency metrics of POD, false alarm rate, and CSI for precipitation in China and eight subregions. Vertical axis scales were set according to the maximum of *y* axis in different subpanels.

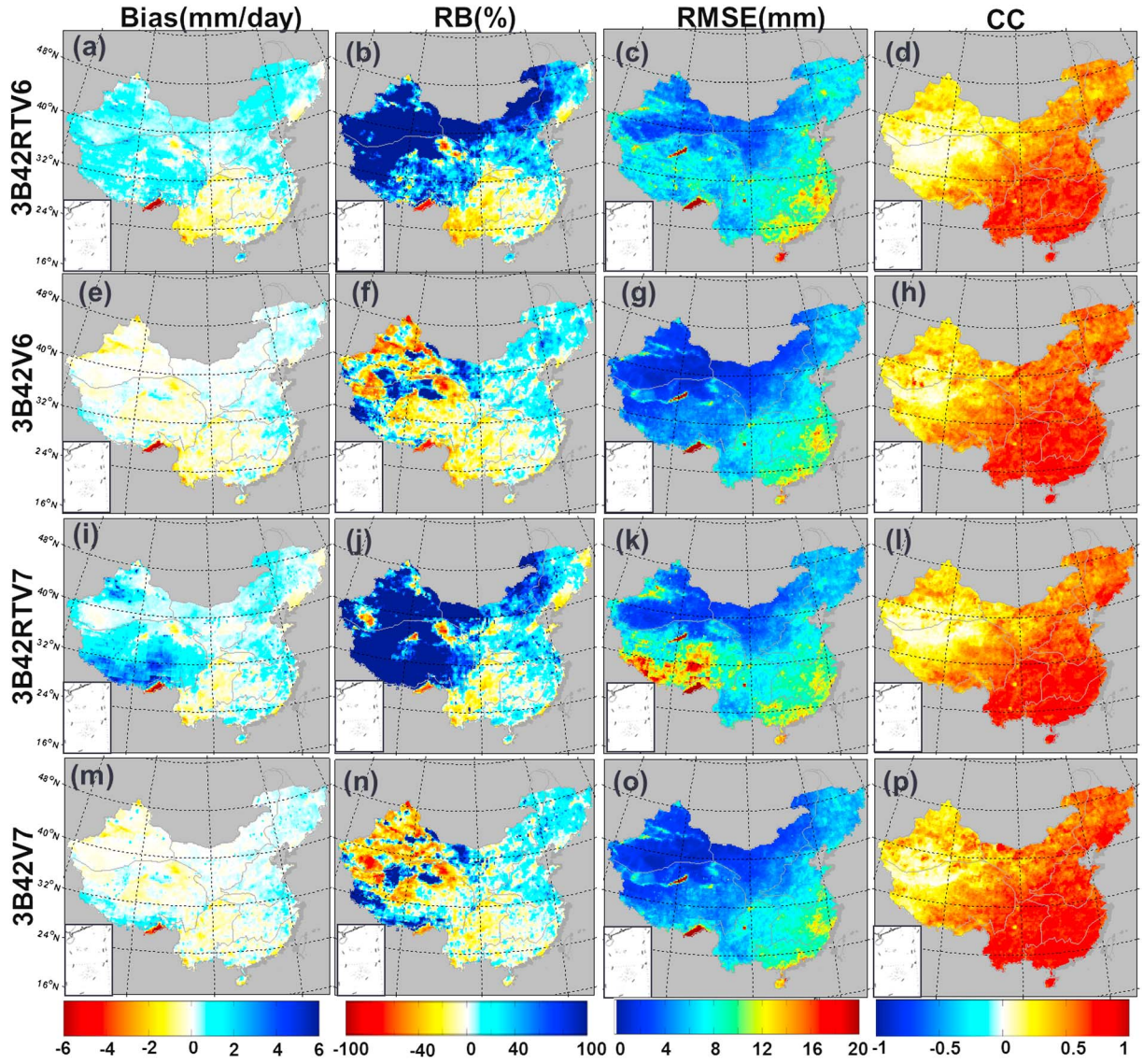

Figure 9. Spatial distributions of Bias, RB, RMSE, and CC for estimated from V6 and V7 TMPA in China.

Nevertheless, according to the statistics of PDFc and PDFv, 3B42V7 slightly outperforms 3B42V6, and 3B42RTV6 performs better than 3B42RTV7.

3.5. Contingency Statistics

[21] Figure 8 shows the performance of V6 and V7 products over China and the eight subregions in terms of probability of detection (POD), critical successful index (CSI), and false alarm rate, with thresholds from 1 to 250 mm/day. Scores with 3B42V6 and 3B42V7 are generally better than the ones for the real-time TMPA products. In particular, 3B42V7 shows the best scores among all products. This is likely a result of the gauge-based correction in TMPA and the addition of SSMI/S. In addition, it is worth noting that all the products have a low POD and CSI when rainfall rates are greater than 50 mm/day in XJ, QZ, and XB. In other regions, 3B42V7 and 3B42V6 give quite better scores than their real-time counterparts when rainfall rates are greater than 100 mm/day, indicating that the real-time TMPA products may have underestimated the extremely heavy rain events.

3.6. Spatial Analysis

[22] The spatial distributions of bias, RB, RMSE, and CC can help hydrologic modelers to anticipate error propagation in hydrological applications. Figure 9 shows the spatial distribution maps of bias, RB, RMSE, and CC of TMPA versus CPAP for 3 year daily mean precipitation. 3B42RTV6 and 3B42RTV7 have similar spatial patterns for statistics of bias, RB, RMSE, and CC. The same trend can be seen for their research products. The real-time products appear to overestimate precipitation in western and northern China (XJ, QZ, XB, DB, and HB) and underestimate it in southern China (YG, CJ, and HN). CC and RMSE decrease from southeastern China to the northwest, except in QZ where 3B42RTV7 shows a much higher RMSE than 3B42RTV6. 3B42V6 and 3B42V7 have a bias close to 0 mm/day in most regions of China, and typically have a positive bias in the southwestern regions of QZ, DB, HB, and the desert areas. They have a negative bias in the mountainous areas in XJ, northwestern QZ, and YG. 3B42RTV7 shows much higher RMSE values (>12 mm) than 3B42RTV6 in QZ, while 3B42RTV6 shows much

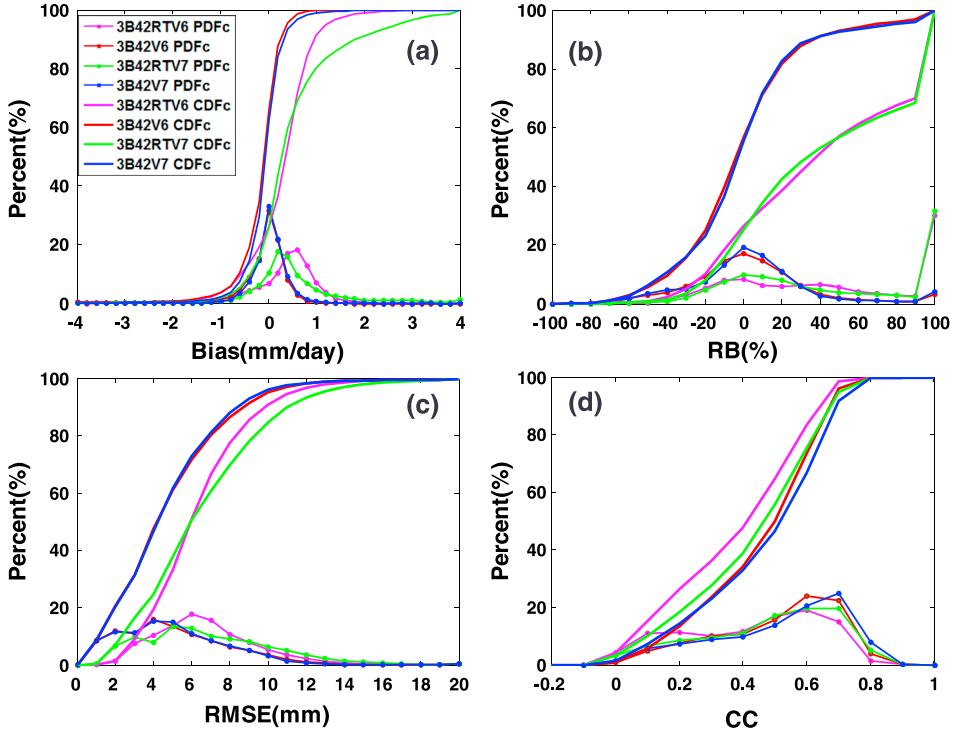

Figure 10. Probability (cumulative) distribution functions PDFc (CDFc) for spatial Bias, RB, RMSE, and CC values shown in Figure 9.

higher RMSE values than 3B42RTV7 in eastern CJ and southeastern HN (i.e., Guangdong and Hainan provinces). This result implies that 3B42RTV7 might not outperform 3B42RTV6 in high-altitude regions (e.g., QZ) but improves the estimation of extremely heavy rainfall in coastal regions (e.g., eastern CJ and HN).

[23] Figure 10 shows the occurrence PDF (PDFc) and occurrence cumulative distribution function (CDFc) of the whole region statistics of bias, RB, RMSE, and CC. As Figure 10 shows, 3B42V6 and 3B42V7 have similar PDFc and CDFc of Bias, RB, RMSE, and CC, although 3B42V7 is slightly better. The difference between 3B42RTV6 and 3B42RTV7 is distinct. The PDFc and CDFc of 3B42RTV7 indicate that the pixels with an estimation bias greater than 0.4 mm/day are apparently more evident than those of 3B42RTV6. A similar conclusion can be drawn for RMSE values greater than 5 mm. To better compare the performance, a set of quantitative numbers for the assessment are given as follows. Regarding 3B42RTV6, 3B42RTV7, 3B42V6, and 3B42V7, the absolute biased precipitation more than 0.5 mm/day accounts for 55.84%, 45.78%, 14.81%, and 13.80%, respectively; the absolute relative biased precipitation more than 20% accounts for 71.54 %, 66.64%, 42.63%, and 40.67%, respectively; the RMSE greater than 6 mm accounts for 58.28%, 54.93%, 33.25%, and 31.96%, respectively; and the CC greater than 0.6 accounts for 26.67 %, 34.49%, 38.37%, and 43.86%, respectively.

4. Summary and Conclusions

[24] The TMPA algorithm incorporates a variety of observations from satellite-based sensors (passive microwave and infrared) and ground-based gauge networks (CPCC "full" gauge analysis) with quasi-global coverage (60°N–60°S for real-time products and 50°N–50°S for research products) at a temporal resolution of 3 h. This paper provides an early and timely quantitative study of error characteristics for the successive V6 and V7 TMPA products in the region of Mainland China, including the real-time product 3B42RT and research product 3B42. The quantitative analysis is based on a comparison with gauge-based CPAP products at multitemporal scales from 3 year mean, seasonal, to daily time series. In addition to the conventional statistical indices, we have conducted frequency and spatial analyses. The main findings of this study are summarized as follows:

[25] 1. Overall, both research products (3B42) have much better performance than the two real-time products (3B42RT) regardless of the version. For the 3 year daily mean precipitation, 3B42V7 has the highest CC (0.93), the lowest RMSE (0.54 mm), and the smallest RB (−0.05%), while 3B42RTV7 has the lowest CC (0.73), the highest RMSE (1.27 mm), and the largest RB (35.84 %); 3B42V6 has a high CC (0.89), a low RMSE (0.69 mm), and a small RB (−4.91%), while 3B42RTV6 has a low CC (0.81), a large RMSE (0.95 mm), and a large RB (21.22%). However, 3B42RTV7 performed better than 3B42RTV6 with less precipitation underestimation and lower RMSE in the moist areas (e.g., CJ and HN).

[26] 2. All TMPA products have low scores of POD and CSI when rainfall rates are greater than 50 mm/day in the arid, western regions. Elsewhere, 3B42V7 and 3B42V6 generally have better scores than their real-time counterparts for extreme rainfall rates greater than 100 mm/day.

[27] 3. V6 and V7 products generally have similar rainfall rate distributions in China by occurrence and volume. Judging by the PDFc and PDFv (Figures 6 and 7), 3B42V7 outperforms 3B42V6, while 3B42RTV6 performs better than 3B42RTV7.

[28] 4. 3B42V7 generally improves upon its predecessor 3B42V6 as shown in the statistics of daily precipitation for 3 years. Particularly, 3B42RTV7 shows much improvement over 3B42RTV6 in southern China, a relatively wet subtropical region. However, it does not yield much improvement in the drier regions in northern and western China, which are characterized by high latitudes (e.g., northeastern China) or high altitudes (e.g., Qinghai-Tibetan plateau).

[29] 5. According to the seasonal analysis, 3B42V7 performs better than 3B42V6 with a higher CC for all seasons (0.94, 0.93, 0.88, and 0.87 for spring, summer, autumn, and winter, respectively) and less underestimation in spring, autumn, and winter (Figure 3).

[30] 6. Both 3B42RTV7 and 3B42RTV6 show distinct overestimation in QZ most of the time. 3B42RTV7 has better skill (i.e., better RB, RMSE, and CC) than 3B42RTV6 during winter, especially in the western, arid regions, and in the north. However, 3B42RTV7 also overestimates in the spring (14.98%), summer (44.24%), and autumn (35.62%). Particularly, 3B42RTV7 overestimates rainfall much more than 3B42RTV6 in the arid XJ region and the high-altitude QZ region in spring, summer, and autumn (Figures 3 and 4 and Table 1).

[31] 7. 3B42RTV7 overestimates daily precipitation more than 3B42RTV6 during the summer and autumn seasons in the western, arid regions, while in winter and spring, 3B42RTV6 overestimates more than 3B42RTV7 here. Correspondingly, 3B42RTV7 shows a higher (lower) RMSE than 3B42RTV6 in summer and autumn (winter and spring). Both versions of 3B42 and 3B42RT show significant underestimation in southwestern YG, especially in summer and autumn. The V6 TMPA products have more underestimation in this region (Figures 3 and 4 and Table 1).

[32] 8. Both 3B42RTV6 and 3B42RTV7 overestimate precipitation in the western, arid regions and in the north, and underestimate in the more humid, southern regions. 3B42RTV7 overestimates more precipitation than 3B42RTV6 in QZ, while it estimates less precipitation in XJ, XB, and DB. 3B42RTV6 (3B42V6) underestimates more precipitation than 3B42RTV7 (3B42V7) in YG, CJ, and HN. All TMPA products show a high RMSE in CJ and HN. 3B42RTV7 shows much higher RMSE (>12 mm) than 3B42RTV6 in QZ, while 3B42RTV6 shows much higher RMSE (>12 mm) than 3B42RTV7 in eastern CJ and southeastern HN.

[33] The error characteristics of the successive V6 and V7 TMPA products are identified and quantified in this study and will have significant implications for hydrological applications in China. The findings on the similarities and differences of 3B42RTV7 and 3B42V7 provide useful feedback to TMPA algorithm developers for further improvement of spaceborne precipitation products. This study confirms the results revealed by *Chen et al*. [2013] in that 3B42V7 shows much improvement over 3B42V6 with a higher correlation coefficient (0.92 over the CONUS and 0.93 over China) and a lower relative bias (−2.37% over the CONUS and −0.05% over China). The real-time product 3B42RTV7 did not show much improvement over 3B42RTV6 [*Chen et al*., 2013]. Although additional efforts are desirable to justify the improvement of V7 TMPA products in other regions of the world, TMPA algorithm developers can have confidence in the quality of the V7 TMPA algorithm as it evolves to the Day 1 algorithm of the GPM mission in 2014.

[34] **Acknowledgments.** We acknowledge the TRMM mission scientists and associated NASA personnel for the production of the data used in this research effort, and are very much indebted to the team responsible for the TMPA products, especially George J. Huffman. Thanks are also given to Youcun Qi of the Cooperative Institute for Mesoscale Meteorological Studies at the University of Oklahoma. This work was financially supported by the NOAA Multifunction Phased-Array Radar project administrated by the Advanced Radar Research Center at the University of Oklahoma.

Reference

Amitai, E., X. Llort, L. Liao, and R. Meneghini (2004), A framework for global verification of space-borne radar estimates of precipitation based on rain type classification, in *2nd TRMM International Science Conference*, edited.

Bajracharya, S., M. Shrestha, P. Mool, and R. Thapa (2008), Validation of satellite rainfall estimation in the summer monsoon dominated area of the Hindu Kush Himalayan region, paper presented at Proc. 4th International Precipitation Working Group Workshop, National Satellite Meteorological Center, Chinese Meteorological Administration.

Behrangi, A., B. Khakbaz, T. C. Jaw, A. AghaKouchak, K. Hsu, and S. Sorooshian (2011), Hydrologic evaluation of satellite precipitation products over a mid-size basin, *J. Hydrol.*, *397*(3), 225–237.

Bothe, O., K. Fraedrich, and X. Zhu (2012), Precipitation climate of Central Asia and the large-scale atmospheric circulation, *Theor. Appl. Climatol.*, *108*(3–4), 345–354.

Chen, M., W. Shi, P. Xie, V. B. S. Silva, V. E. Kousky, R. W. Higgins, and J. E. Janowiak (2008), Assessing objective techniques for gauge-based analyses of global daily precipitation, *J. Geophys. Res.*, *113*, D04110, doi:10.1029/2007JD009132.

Chen, G., W. Sha, and T. Iwasaki (2009), Diurnal variation of precipitation over southeastern China: Spatial distribution and its seasonality, *J. Geophys. Res.*, *114*, D13103, doi:10.1029/2008JD011103.

Chen, S., P. E. Kirstette, Y. Hong, J. Gourley, J. Zhang, K. Howard, and J. Hu (2012a), Quantification of spatial errors of precipitation rates and types from the TRMM precipitation radar (the latest successive V6 and V7) over the United States. Presentation, paper presented at AGU Fall meeting, San Francisco, 3–7 December 2012.

Chen, S., Y. Hong, Q. Cao, P.-E. Kirstetter, J. J. Gourley, Y. Qi, J. Zhang, K. Howard, J. Hu, and J. Wang (2012b), Performance evaluation of radar and satellite rainfalls for Typhoon Morakot over Taiwan: Are remote-sensing products ready for gauge denial scenario of extreme events?, *J. Hydrol.*, doi:10.1016/j.jhydrol.2012.12.026.

Chen, S., et al. (2013), Evaluation of the successive V6 and V7 TRMM multisatellite precipitation analysis over the Continental United States, *Water Resour. Res.*, *49*, doi:10.1002/2012WR012795.

Dai, A. (2006), Precipitation characteristics in eighteen coupled climate models, *J. Clim.*, *19*(18), 4605–4630.

Daly, C., R. P. Neilson, and D. L. Phillips (1994), A statistical-topographic model for mapping climatological precipitation over mountainous terrain, *J. Appl. Meteorol.*, *33*(2), 140–158.

Ferraro, R. R., E. A. Smith, W. Berg, and G. J. Huffman (1998), A screening methodology for passive microwave precipitation retrieval algorithms, *J. Atmos. Sci.*, *55*(9), 1583–1600.

Fu, Y., and G. Liu (2007), Possible misidentification of rain type by TRMM PR over Tibetan Plateau, *J. Appl. Meteorol. Climatol.*, *46*(5), 667–672.

Gjertsen, U., and G. Haase (2005), Radar data quality—The challenge of beam blockages and propagation changes, paper presented at Proceedings of the WMO/Météo-France WWRP Symposium on Nowcasting and Very Short Range Forecasting.

Gourley, J. J., Y. Hong, Z. L. Flamig, L. Li, and J. Wang (2010), Intercomparison of rainfall estimates from radar, satellite, gauge, and combinations for a season of record rainfall, *J. Appl. Meteorol. Climatol.*, *49*(3), 437–452.

Grody, N. C. (1991), Classification of snow cover and precipitation using the special sensor microwave imager, *J. Geophys. Res.*, *96*(D4), 7423–7435.

Grody, N. C., and F. Weng (2008), Microwave emission and scattering from deserts: Theory compared with satellite measurements, *IEEE Trans. Geosci. Remote Sens.*, *46*(2), 361–375.

Hirpa, F. A., M. Gebremichael, and T. Hopson (2010), Evaluation of high-resolution satellite precipitation products over very complex terrain in Ethiopia, *J. Appl. Meteorol. Climatol.*, *49*(5), 1044–1051.

Huffman, G. J., and D. T. Bolvin (2013), TRMM and other data precipitation data set documentation, *Laboratory for Atmospheres*, *NASA Goddard Space Flight Center and Science Systems and Applications*. ftp://precip.gsfc.nasa.gov/pub/trmmdocs/3B42_3B43_doc.pdf.

Huffman, G. J., D. T. Bolvin, E. J. Nelkin, D. B. Wolff, R. F. Adler, G. Gu, Y. Hong, K. P. Bowman, and E. F. Stocker (2007), The TRMM multisatellite precipitation analysis (TMPA): Quasi-global, multiyear, combined-sensor precipitation estimates at fine scales, *J. Hydrometeorol.*, *8*(1), 38–55.

Huffman, G. J., R. F. Adler, D. T. Bolvin, E. J. Nelkin, F. Hossain, and M. Gebremichael (2010), The TRMM multi-satellite precipitation analysis (TMPA), *Satell. Rainfall Appl. Surf. Hydrol.*, 3–22.

Huffman, G. J., D. T. Bolvin, E. J. Nelkin, and R. F. Adler (2011), Highlights of Version 7 TRMM Multi-satellite Precipitation Analysis (TMPA), *5th Internat. Precip. Working Group Workshop, Workshop Program and Proceedings, 11–15 October 2010, Hamburg, Germany. C. Klepp and G. Huffman Eds. Reports on Earth Sys. Sci., 100/2011, Max-Planck-Institut für Meteorologie. ISSN* 1614-1199, 109-110.

Iguchi, T., R. Meneghini, J. Awaka, T. Kozu, and K. Okamoto (2000), Rain profiling algorithm for TRMM precipitation radar data, *Adv. Space Res.*, *25*(5), 973–976.

Jiang, H., and E. J. Zipser (2010), Contribution of tropical cyclones to the global precipitation from eight seasons of TRMM data: Regional, seasonal, and interannual variations, *J. Clim.*, *23*(6), 1526–1543.

Kidd, C., and G. Huffman (2011), Global precipitation measurement, *Meteorol. Appl.*, *18*(3), 334–353.

Kirstetter, P.-E., Y. Hong, J. Gourley, M. Schwaller, W. Petersen, and J. Zhang (2013), Comparison of TRMM 2A25 Products, Version 6 and Version 7 with NOAA/NSSL Ground Radar-Based National Mosaic QPE, *J. Hydrometeorol.*, *14*(2), 661–669.

Li, L., C. S. Ngongondo, C.-Y. Xu, and L. Gong (2013), Comparison of the global TRMM and WFD precipitation datasets in driving a large-scale hydrological model in Southern Africa, *Hydrol. Res.*, doi:10.2166/nh.2012.175.

Liang, J. (2012), Study of the influences of monsoon gyres on formation and sudden track change of typhoons, Dissertation thesis, College of Atmospheric Science, Nanjing University of Information Science & Technology, China.

Negri, A. J., and R. F. Adler (1993), An intercomparison of three satellite infrared rainfall techniques over Japan and surrounding waters, *J. Appl. Meteorol.*, *32*(2), 357–373.

Parkes, B., F. Wetterhall, F. Pappenberger, Y. He, B. Malamud, and H. Cloke (2013), Assessment of a 1-hour gridded precipitation dataset to drive a hydrological model: A case study of the summer 2007 floods in the Upper Severn, UK, *Hydrol. Res.*, *44*(1), 89–105.

Qian, W., and X. Lin (2005), Regional trends in recent precipitation indices in China, *Meteorol. Atmos. Phys.*, *90*(3), 193–207.

Sakakibara, H. (1981), Heavy rainfall from very shallow convective clouds, *J. Meteorol. Soc. Japan*, *59*, 387–394.

Shen, Y., M. Feng, H. Zhang, and F. Gao (2010a), Interpolation methods of China daily precipitation data, *J. Appl. Meteorol. Sci. (Chinese)*, *21*(3), 279–281.

Shen, Y., A. Xiong, Y. Wang, and P. Xie (2010b), Performance of high-resolution satellite precipitation products over China, *J. Geophys. Res.*, *115*, D02114, doi:10.1029/2009JD012097.

Shepherd, J. M. (2006), Evidence of urban-induced precipitation variability in arid climate regimes, *J. Arid Environ.*, *67*(4), 607–628.

Shige, S., S. Kida, H. Ashiwake, T. Kubota, and K. Aonashi (2012), Improvement of TMI rain retrievals in mountainous areas, *J. Appl. Meteorol. Climatol.*, *52*(1), 242–254.

Smith, R. A., and C. D. Kummerow (2013), A comparison of in-situ, reanalysis, and satellite water budgets over the Upper Colorado River Basin, *J. Hydrometeorol.*, *14*(3), 888–905.

Sorooshian, S. (2004), Commentary-GEWEX (Global Energy and Water Cycle Experiment) at the 2004 joint scientific committee meeting, *GEWEX Newsl*, *14*(2), 2.

Stampoulis, D., and E. N. Anagnostou (2012), Evaluation of global satellite rainfall products over Continental Europe, *J. Hydrometeorol.*, *13*(2), 588–603.

Story, G. J., H. Forecaster, and W. G. R. F. Center (2001), *Determining WSR-88D Precipitation Algorithm Performance Using the Stage III Precipitation Processing System*, pp. 14, West Gulf River Forecast Center, Fort Worth, TX.

Surussavadee, C., and D. H. Staelin (2010), Correcting microwave precipitation retrievals for near-surface evaporation, paper presented at Geoscience and Remote Sensing Symposium (IGARSS), 2010 IEEE International, 25–30 July 2010.

Takao, T., and T. Kunio (1980), Radar observation of rainfall system modified by orographic effects, *J. Meteor. Soc. Japan*, *58*, 500–516.

Tang, Z., Z. Wang, C. Zheng, and J. Fang (2006), Biodiversity in China's mountains, *Front. Ecol. Environ.*, *4*(7), 347–352.

Tapiador, F. J., J. Turk, W. Petersen, A. Y. Hou, E. García-Ortega, L. A. T. Machado, C. F. Angelis, P. Salio, C. Kidd, and G. J. Huffman (2012), Global precipitation measurement: Methods, datasets and applications, *Atmos. Res.*, *104–105*, 70–97.

Tian, Y., C. D. Peters-Lidard, B. J. Choudhury, and M. Garcia (2007), Multitemporal analysis of TRMM-based satellite precipitation products for land data assimilation applications, *J. Hydrometeorol.*, *8*(6), 1165–1183.

Tian, Y., C. D. Peters-Lidard, R. F. Adler, T. Kubota, and T. Ushio (2010), Evaluation of GSMaP precipitation estimates over the contiguous United States, *J. Hydrometeorol.*, *11*(2), 566–574.

Tobin, K. J., and M. E. Bennett (2009), Using SWAT to model streamflow in two river basins with ground and satellite precipitation data1, *J. Am. Water Resour. Assoc.*, *45*(1), 253–271.

Todd, M. C., and J. O. Bailey (1995), Estimates of rainfall over the United Kingdom and surrounding seas from the SSM/I using the polarization corrected temperature algorithm, *J. Appl. Meteorol.*, *34*(6), 1254–1265.

Tuttle, J. D., R. E. Carbone, and P. A. Arkin (2008), Comparison of ground-based radar and geosynchronous satellite climatologies of warm-season precipitation over the United States, *J. Appl. Meteorol. Climatol.*, *47*(12), 3264–3270.

Vicente, G. A., R. A. Scofield, and W. P. Menzel (1998), The operational GOES infrared rainfall estimation technique, *Bull. Am. Meteorol. Soc.*, *79*(9), 1883–1898.

Vila, D., R. Ferraro, and R. Joyce (2007), Evaluation and improvement of AMSU precipitation retrievals, *J. Geophys. Res.*, *112*, D20119, doi:10.1029/2007JD008617.

Yong, B., L. L. Ren, Y. Hong, J. H. Wang, J. J. Gourley, S. H. Jiang, X. Chen, and W. Wang (2010), Hydrologic evaluation of multisatellite precipitation analysis standard precipitation products in basins beyond its inclined latitude band: A case study in Laohahe basin, China, *Water Resour. Res*, *46*, W07542, doi:10.1029/2009WR008965.

Yong, B., Y. Hong, L. L. Ren, J. J. Gourley, G. J. Huffman, X. Chen, W. Wang, and S. I. Khan (2012), Assessment of evolving TRMM-based multisatellite real-time precipitation estimation methods and their impacts on hydrologic prediction in a high latitude basin, *J. Geophys. Res.*, *117*, D09108, doi:10.1029/2011JD017069.

Zhou, T., R. Yu, H. Chen, A. Dai, and Y. Pan (2008), Summer precipitation frequency, intensity, and diurnal cycle over China: A comparison of satellite data with rain gauge observations, *J. Clim.*, *21*(16), 3997–4010.